J Mater Sci (2024) 59:978–990

Materials for life sciences

Investigation of the electrochemical behavior of a newly designed TiMg dental implant

Ahmed Mohamed Hassan Ibrahim[1,2,3,*] and Martin Balog[1,2]

[1] *Centre of Excellence for Advanced Materials Application, The Slovak Academy of Sciences, Dubravska Cesta 9, 84511 Bratislava, Slovakia*
[2] *Institute of Materials and Machine Mechanics, The Slovak Academy of Sciences, Dubravska Cesta 9, 84513 Bratislava, Slovakia*
[3] *Physics Department, Faculty of Science, Mansoura University, Mansoura 35516, Egypt*

Received: 7 July 2023
Accepted: 24 November 2023
Published online: 16 December 2023

ABSTRACT

This study is aimed to evaluate the galvanic corrosion of a newly designed TiMg dental implant. The TiMg composite was tested in two forms: (1) cylinders (TiMg cyl) and (2) dental implants (TiMg DI). Surface roughness was measured using a confocal microscope. The electrochemical behavior was determined in a Hank's balanced salt solution (HBSS) by the open-circuit potential (OCP), potentiodynamic polarization (PDP), and electrochemical impedance spectroscopy (EIS) measurements. Surfaces after corrosion were examined by a scanning electron microscope (SEM) equipped with an energy-dispersive X-ray spectrometer (EDS). OCP of TiMg cyl and TiMg DI increased in the noble direction, indicating the formation and growth of a base film on their surfaces. After 2-h immersion, TiMg cyl had higher values of i_{Corr} and R_{Corr} compared with those of TiMg DI. After 24-h immersion, a prominent reduction in the values of i_{Corr} and R_{Corr} was observed, and E_{Corr} shifted positively. The Nyquist plots of TiMg cyl and TiMg DI show capacitive loops that tended to close after 2-h exposure. As the time extended, TiMg DI showed higher corrosion resistance compared with that of TiMg cyl, and the linear diffusion response arose from the formation and dissolution of chemically non-stable by-products caused by the hydrogen evolution. In such a case, the involved reaction was controlled by charge transfer and diffusion processes. The formation of a film composed of stable CAp species that attached directly to the surface and chemically non-stable by-products that included ($Mg_3(PO_4)_2$) and $Mg(OH)_2$ was demonstrated. To conclude, the obtained results revealed that TiMg DI of a complicated threaded design had a more stable passive film and higher corrosion resistance in HBSS compared with those of TiMg cyl of a cylindrical design. These findings have the utmost importance for the fabrication of dental implants.

Handling Editor: Annela M. Seddon.

Address correspondence to E-mail: ahmed.ibrahim@savba.sk

https://doi.org/10.1007/s10853-023-09199-4

GRAPHICAL ABSTRACT

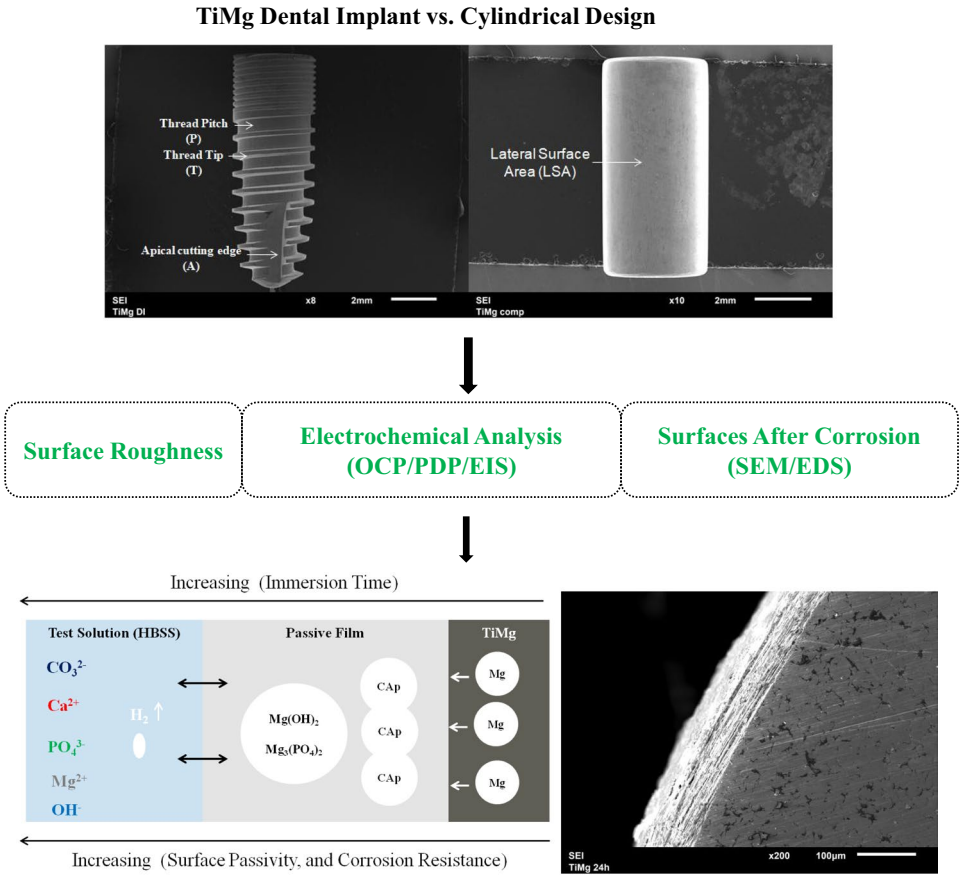

Introduction

Although titanium (Ti) and Ti-based alloys are the most widespread materials for dental implant fabrication and used with a successful rate [1, 2], two main issues are of particular concern: (1) a mismatch in Young's modulus (E) between the bone and implants and (2) insufficient surface bioactivity of implants [2]. The composite, namely the one with a Ti+17 vol% Mg composition, was introduced as a promising candidate in our previous works [3–6] to minimize the above-mentioned drawbacks of currently used Ti-based materials. Its Ti matrix assures required mechanical properties under static and dynamic loading, and the biodegradable Mg component leads to a reduction in E and promotes bone deposition and osseointegration [7–9]. Mechanical treatment by grinding and polishing was applied for the surface finish of the Ti+17 vol% Mg composite of a cylindrical design, as was demonstrated in [6]. The smooth and less strained surface resulted in a pronounced response represented by a tolerated degradation rate and a distinct in vitro biological behavior [6]. Moreover, it eliminated the need for further surface treatments, e.g., sandblasting, chemical etching, etc., and concurrently maintained the bioactive surface nature when compared with the established Ti-based materials.

Although most orthopedic implants are susceptible to a variety of corrosion processes, galvanic corrosion is of particular concern. The galvanic corrosion occurs when two (or more) dissimilar metals are coupled in a corrosive medium. In the case of dental implants, when saliva penetrates prosthetic components, the less noble metal corrodes at an accelerated rate, resulting in a flow of electric current. This current flows through the surrounding tissues and thus causes some pain

and local inflammation [10–12]. The overall rate of electrochemical processes involved in a dental implant structure is mainly linked to the formation of a base film at the interface and the transport of either metal or oxygen through the formed film [13]. Mg is prone to corrosion in aqueous solutions because of its high chemical activity, i.e., a low standard electrode potential (− 2.356 V) [14]. Mg and its alloys were used in conjunction with different components, such as aluminum, steel, zinc, carbon fiber, and copper [14–19]. In specific environments, such materials exhibited an accelerated rate of Mg degradation due to the galvanic coupling. For the Ti+17 vol% Mg composite material, the contact between Mg and Ti is susceptible to the galvanic corrosion in the oral environment due to a high difference in their standard electrode potential (− 2.356 vs. − 0.163, respectively) [20, 21]. Therefore, it is inevitable to study the galvanic corrosion behavior and mechanism of the proposed material.

Several techniques were used to investigate the galvanic corrosion of dental implant materials, such as potentiodynamic polarization (PDP) and electrochemical impedance spectroscopy (EIS) [22, 23]. The PDP measurements give information about the corrosion potential (E_{corr}), which expresses the thermodynamic stability of the studied systems and the resistance of materials against corrosion [24, 25]. The corrosion kinetics are linked to the corrosion rate (R_{Corr}), which can be calculated from the corrosion current density (i_{corr}). But EIS helps in the evaluation of corrosion mechanism, corrosion resistance, and surface passivity [25–29]. It measures the resistance of a metal/electrolyte interface over a wide range of frequencies (from 100 mHz to 100 kHz). Moreover, it precisely characterizes the systems formed by an array of layers with different properties by employing electrical equivalent models. These models allow a correlation between the applied electrical elements and processes that may occur in the studied systems.

The purpose of this study was the evaluation of electrochemical (galvanic) corrosion properties of a dental implant (DI) fabricated from the newly designed Ti+17 vol% Mg composite material (further labeled as TiMg). Corrosion properties of DI were examined using the open-circuit potential (OCP), PDP, and EIS measurements to understand the corrosion behavior and mechanism in a simulated physiological environment. The present study was performed using a commercial design MV3.6-10 DI in Hank's balanced salt solution (HBSS) in line with the ASTM G5-14 and ISO 10993-15 guidelines to mimic the performance upon the desired application. The obtained results were directly compared with those of the TiMg composite of a cylindrical design to evaluate how various surface characteristics, e.g., geometry, roughness, and Mg forms, influenced the degradation of Mg in the test solution.

Experimental

Materials

The TiMg composite was fabricated from plasma atomized (PA) Ti Grade 1 (AP&C, Canada) and gas atomized (GA) Mg (IMR Metalle, Austria) powders by a powder metallurgy approach, which consisted of blending, cold isostatic pressing (CIP) at a pressure of 200 MPa, uniaxial hot vacuum pressing (HVP) at a pressure of 500 MPa, a vacuum of 8 Pa, and a temperature of 410 °C and eventually direct extrusion (DE) at a reduction ratio of 16:1, a ram speed of 10 mm s^{-1}, and the extrusion temperature was set to 420 °C. The TiMg composite material was tested in two forms: (1) cylinders (labeled as TiMg cyl) and (2) dental implants (labeled as TiMg DI). Cylindrical samples had a diameter of 4 mm and a height of 8 mm and were machined longitudinally to the extruded rods. The as-machined cylinders were ground using abrasive grits (up to 4000# grit size) and then polished using abrasive diamond paste with a size of 1 µm to obtain a fine and smooth surface, as was described in [6]. The TiMg DI samples were a commercial design MV3.6-10 DI [30] with a thread diameter of 3.6 mm and a length of 10 mm. The TiMg DI samples were produced using a common computer numerical controlled (CNC) machining approach that is typically used to produce commercial Ti-based dental implants without any surface treatments. All samples were ultrasonically cleaned in ethanol, air-dried, and finally stored in a desiccator for coveted tests.

Surface roughness measurement

The surface roughness of the TiMg cyl and TiMg DI samples was measured using a ZEISS LSM 700 confocal microscope (Carl Zeiss Microscopy GmbH, Germany) according to the ISO 25178 guidelines. 3D-colored maps of the investigated surfaces were processed using ConfoMap ST software. Two surface areas of interest (SA1 and SA2) on the lateral side of TiMg cyl with an area

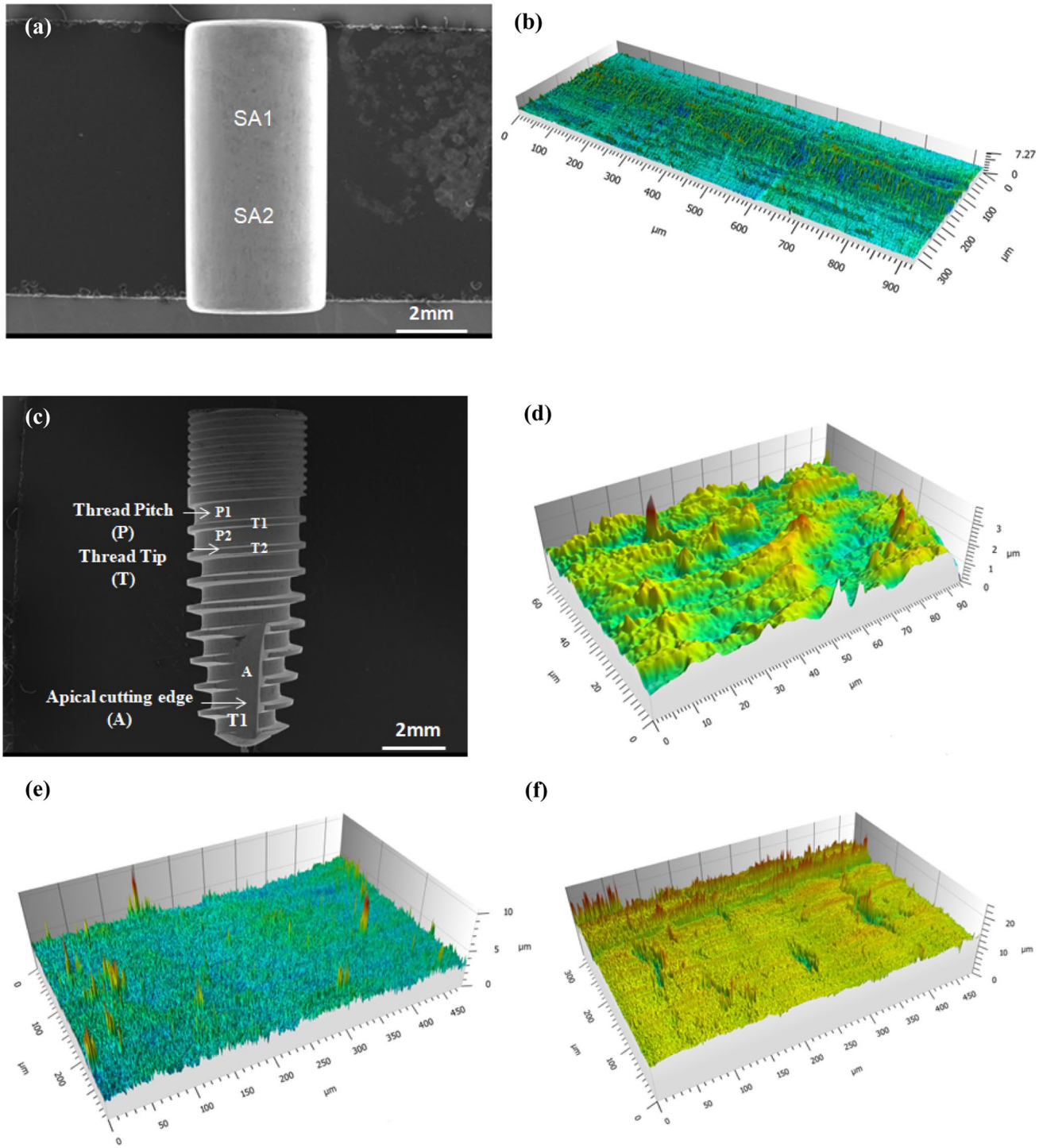

Figure 1 **a** SEM micrograph of the lateral surface of TiMg cyl that displays areas of interest (SA1 and SA2) for surface roughness measurement. **b** 3D-colored map of the representative surface area (SA1) of TiMg cyl. **c** SEM micrograph of MV3.6-10 TiMg DI that displays areas of interest on the thread pitch (*P*1 and *P*2), the thread tip (T1 and T2), and the apical cutting edge (*A*) for surface roughness measurement. 3D-colored maps of the representative surface areas **d** *T*1, **e** *A*, and **f** *P*1 of TiMg DI.

of 320 × 920 μm^2 for each one were examined (Fig. 1a). But five areas of interest on a thread pitch (*P*1 and *P*2), a thread tip (*T*1 and *T*2), and apical cutting edge (*A*) of TiMg DI were analyzed (Fig. 1c). The scanned areas were 480 × 320 μm^2 for *P*1 and *P*2, 96 × 64 μm^2 for *T*1 and *T*2, and 298 × 480 μm^2 for *A*. The surface roughness parameters that included arithmetical mean height (Sa), root mean square height (Sq), and maximum height (Sz) were determined for the measured areas. The obtained data were expressed as mean ± standard deviation (SD).

Electrochemical measurements

To mimic the in vivo environment, HBSS was used in all experiments. The chemical composition of HBSS is reported in Table 1. The experiments were performed at 37 ± 0.5 °C and the pH was adjusted to 7.4. Electrochemical measurements were performed on a VersaSTAT3 potentiostat (AMETEK, Inc., USA), controlled by VersaStudio software, following the ASTM G5-14 and ISO 10993-15 guidelines with minor changes. A three-electrode cell (K47, Princeton Applied Research) containing 900 mL HBSS was used. In the cell, twin graphite counter electrodes and a saturated calomel reference electrode (SCE) (Hg/$HgCl_2$/saturated KCl) were employed. The top and bottom flat sides of the TiMg cyl samples were covered with a silicone adhesive, leaving a 1-cm^2 surface area exposed to the test solution. But only the top side of the TiMg DI samples was covered, leaving an exposed surface area of 1.8 cm^2. The sample holder was inserted into a threaded hole on the top side of the TiMg cyl and TiMg DI samples. Both samples were vertically positioned and entirely immersed in the electrolyte as a working electrode. The OCP variation was recorded over the first 2-h immersion in HBSS. A scan rate of 0.5 mV/s was applied for PDP, and each test was carried out in the range of − 250 mV below OCP to 500 mV above. The PDP scans were performed after the tested samples were immersed in HBSS for 2 and 24 h. The parameters *βa*, *βc* (anodic and cathodic Tafel slopes, respectively), E_{Corr}, i_{Corr}, and R_{Corr} were obtained from the PDP curves using CView 3.5 software program (Scribner Associates Inc., USA). For EIS, a frequency range of 100 kHz to 100 mHz was applied, and the perturbation amplitude was 10 mV. Similar to PDP, the scans were performed after the samples were exposed to HBSS for 2 and 24 h. For the PDP and EIS measurements after 24-h exposure, the OCP value was detected automatically by the potentiostat at the moment at which the measurements started. Equivalent electrical models were proposed by ZSimpWin 3.20 software to fit the obtained EIS data. All measurements were repeated three times to assure reproducibility. After corrosion testing, the surfaces of TiMg cyl and TiMg DI and the formed base film were analyzed using a scanning electron microscope (SEM, JEOL JSM-6610) equipped with an energy-dispersive X-ray spectrometer (EDS, Oxford).

Results

Evaluation of surface roughness

Figure 1 presents SEM micrographs of surfaces of the TiMg cyl and TiMg DI samples along with 3D-colored maps of the representative surface areas of both samples. The mean values of surface roughness parameters for TiMg cyl were slightly smaller compared with those of TiMg DI. The surface roughness parameters for the representative areas of TiMg DI were different. The surface of the thread tip had the smoothest roughness parameters, while the surface of the thread pitch was rather rough, as shown in Fig. 1d and f. Furthermore, the surface of the apical cutting edge had almost similar roughness parameters to those of the lateral surface of TiMg cyl (Fig. 1b, e). The corresponding roughness parameters, sa, sq, and sz, for the scanned surface areas of TiMg cyl (SA1 and SA2) and TiMg DI (*T*1, *T*2, *A*, *P*1, and *P*2) are given in Table 2.

Open-circuit potential (OCP)

Figure 2 shows curves of OCP versus exposure time of the TiMg cyl and TiMg DI samples immersed in HBSS for 2 h at 37 °C. The 2-h interval was selected since it was sufficient time for the surfaces of the studied samples to form a base film. The OCP variation with time was almost similar for both samples without any significant differences. In the initial stages of immersion (first

Table 1 Chemical composition of Hank's balanced salt solution

Component	NaCl	KCl	$CaCl_2$	$MgSO_4{\cdot}7H_2O$	$MgCl_2{\cdot}6H_2O$	Na_2HPO_4	KH_2PO_4	Glucose	$NaHCO_3$
Fraction, mg L^{-1}	8000	400	140	100	100	60	60	1000	350

Table 2 The corresponding surface roughness parameters for the scanned areas of TiMg cyl (SA1 and SA2) and TiMg DI (*T*1, *T*2, *A*, *P*1, and *P*2)

Sample	Scanned area	Parameter (μm)		
		Sa	Sq	Sz
TiMg cyl	SA1	0.376	0.49	7.09
	SA2	0.347	0.476	7.27
	Mean ± SD	0.361 ± 0.019	0.483 ± 0.009	7.18 ± 0.127
TiMg DI	*T*1	0.211	0.27	3.81
	*T*2	0.228	0.299	3.34
	A	0.329	0.449	10.6
	*P*1	0.888	1.35	24.3
	*P*2	0.987	1.54	24.8
	Mean ± SD	0.527 ± 0.377	0.782 ± 0.613	13.37 ± 10.6

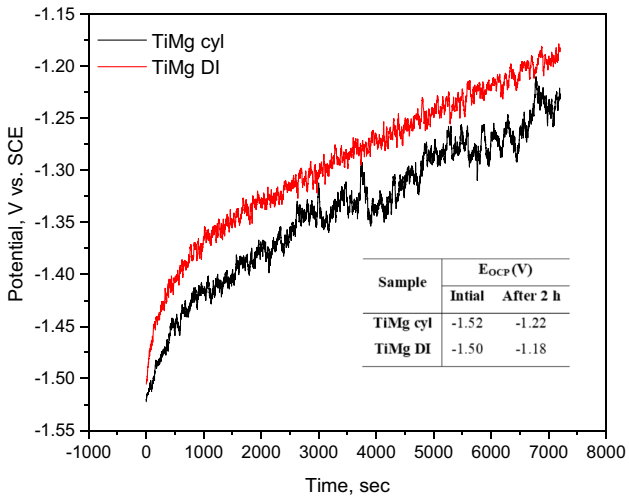

Figure 2 The open-circuit potential (OCP) variation with exposure time for the TiMg cyl and TiMg DI samples immersed in HBSS for 2 h at 37 °C along with the OCP values at the moment at which the experiments started, and 2 h later.

~ 15 min), an abrupt displacement of OCP occurred toward the positive (noble) direction. Afterward, OCP increased slowly with extending the exposure time. Apart from that, some considerable fluctuations in the OCP curve occurred for TiMg cyl.

Potentiodynamic polarization (PDP)

Figure 3 shows PDP curves of the TiMg cyl and TiMg DI samples after 2- and 24-h immersion in HBSS at 37 °C. The parameters βa, βc, E_{Corr}, i_{Corr}, and R_{Corr} that were obtained from the PDP curves are presented in Table 3. After 2-h immersion, both samples exhibited high corrosion tendencies in the test solution, and TiMg cyl had slightly higher values of i_{Corr} and R_{Corr}

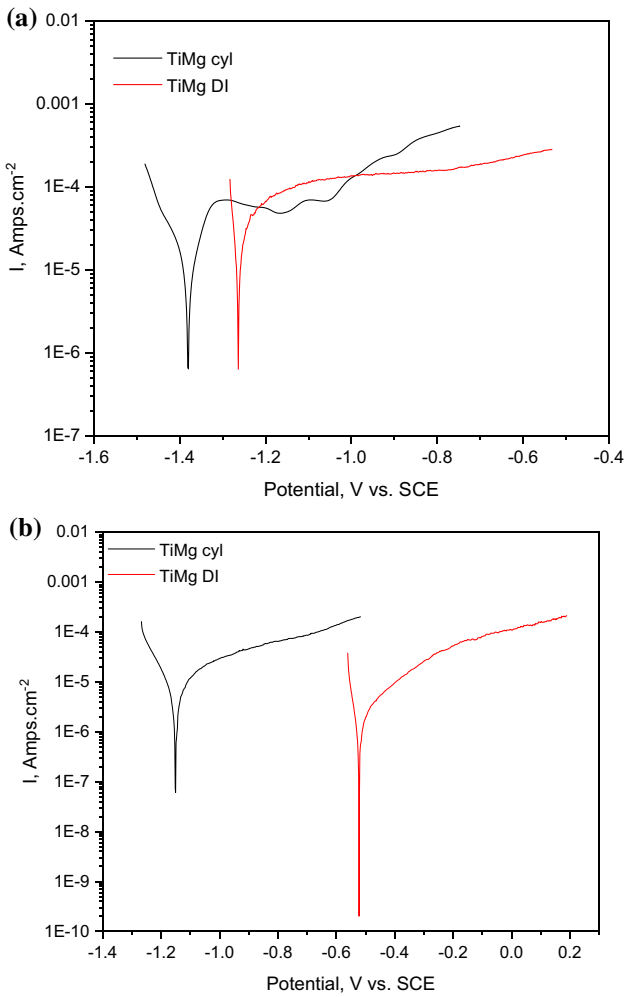

Figure 3 Potentiodynamic polarization (PDP) curves of the TiMg cyl and TiMg DI samples after a) 2- and b) 24-h immersion in HBSS at 37 °C.

Table 3 The parameters βa, βc (anodic and cathodic Tafel slopes, respectively), E_{Corr} (corrosion potential), i_{Corr} (corrosion current), and corrosion rate (R_{Corr}) that were obtained from the potentiodynamic polarization (PDP) curves of the TiMg cyl and TiMg DI samples after 2- and 24-h immersion in HBSS at 37 °C

Sample	Immersion time (h)	β_a (mV)	β_c (mV)	i_{Corr} (A cm^{-2})	E_{Corr} (mV)	R_{Corr} (mmpy)
TiMg cyl	2	477	404	6.86×10^{-5}	−1.387	0.67742
	24	265	99	9.97×10^{-6}	−1.097	0.09841
TiMg DI	2	354	47	4.39×10^{-5}	−1.264	0.43331
	24	166	44	1.79×10^{-6}	−0.522	0.01768

compared with those of TiMg DI. Moreover, TiMg cyl had a higher value of βc compared with that of TiMg DI, indicating a huge release of H_2 bubbles due to the dissolution of Mg. After 24-h immersion, a reduction in the values of i_{Corr} and R_{Corr} was observed, and E_{Corr} shifted positively. The reduction was significant, particularly for TiMg DI, whereby R_{Corr} of TiMg cyl and TiMg DI was 0.09841 and 0.01768 mmpy, respectively. For both samples, βa had higher values than those of βc. This revealed an anodic control during the corrosion process.

Electrochemical impedance spectroscopy (EIS)

Figure 4 shows Nyquist plots of the TiMg cyl and TiMg DI samples after 2- and 24-h immersion in HBSS at 37 °C. The Nyquist plots that represent the EIS data were analyzed by employing electrical equivalent models, as shown in Fig. 5. The proposed models consisted of the resistance of the test solution (Rs), a constant phase element (CPE1) that represented the capacitance response of the formed film, the dispersion coefficient of the formed film ($n1$), the resistance of the formed film ($R1$), the double layer capacitance (CPEdl), the dispersion coefficient of the double layer (ndl), the charge transfer resistance (Rct), and Warburg impedance (W) that represented the impedance arising from the mass transfer and chemical diffusion processes. Model (a) and model (b) were used to fit the EIS data obtained after 2- and 24-h immersion, respectively. The EIS experimental data and the proposed equivalent models matched very well (Chi-square $\chi^2 < 10^{-4}$). The Nyquist plots (Fig. 4a) show capacitive loops that tended to close for both samples immersed in HBSS for 2 h. After 24-h immersion, non-closing capacitive loops were observed, and the EIS data showed higher corrosion resistance (i.e., higher values of R1). Moreover, n1 had lower values for TiMg cyl and TiMg DI, and the values of ndl for TiMg cyl were higher than those of TiMg DI. Furthermore, with extending the exposure time, TiMg cyl and TiMg DI

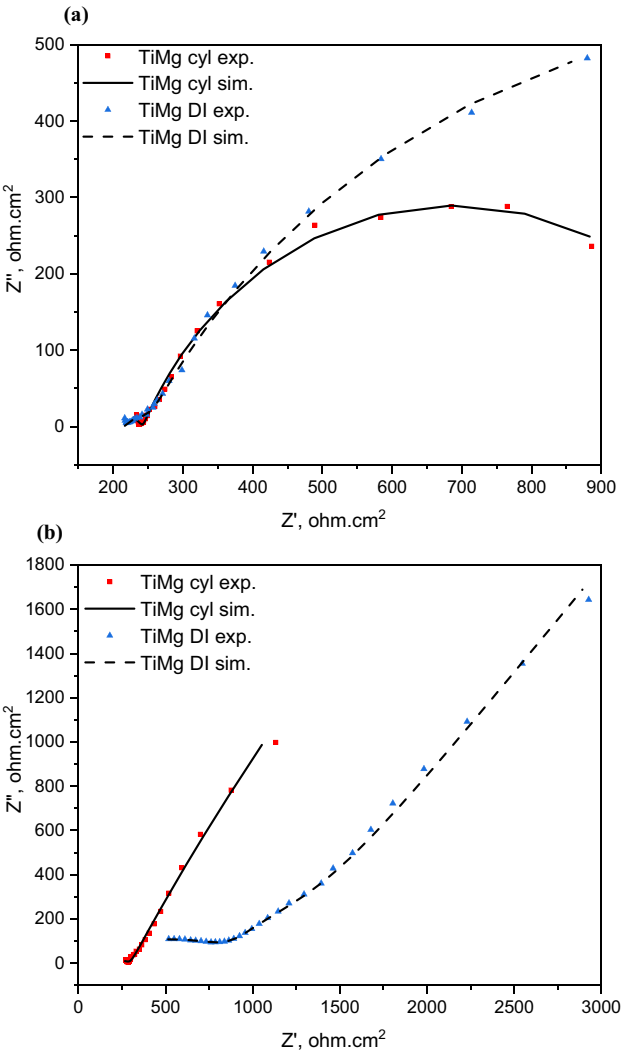

Figure 4 Experimental and simulated Nyquist plots of the TiMg cyl and TiMg DI samples after **a** 2- and **b** 24-h immersion in HBSS at 37 °C.

had an extremely low Rct, and the Warburg impedance was visible in the Nyquist plots as a straight line in the low frequency region (Fig. 4b). The corresponding values of parameters of the equivalent models are presented in Table 4. It is worth pointing out that the EIS data were consistent with the results obtained by the PDP measurements.

Figure 6 shows the mechanism of Mg degradation of the TiMg composite. The Mg degradation resulted in the formation of charge-deficient sites at the surface of the studied sample. As a result, distinct species, such as Ca, P, and carbonate, were incorporated from the test solution into the surface. The corrosion by-products are mainly carbonated apatite species CAp ($Ca_5(PO_4/CO_3)_3(OH)$), magnesium phosphate ($Mg_3(PO_4)_2$), and magnesium hydroxide $Mg(OH)_2$, as was confirmed in our previous studies [3–6].

Examination of surfaces after corrosion

Figure 7 shows SEM micrographs of surfaces of the TiMg cyl and TiMg DI samples after 2- and 24-h exposure to HBSS at 37 °C. The surfaces of the studied samples were almost fully covered in corrosion by-products after 24-h immersion when compared with 2-h immersion. The base film that formed on the surface of the TiMg cyl sample was thicker and grew uniformly after 24-h exposure when compared with

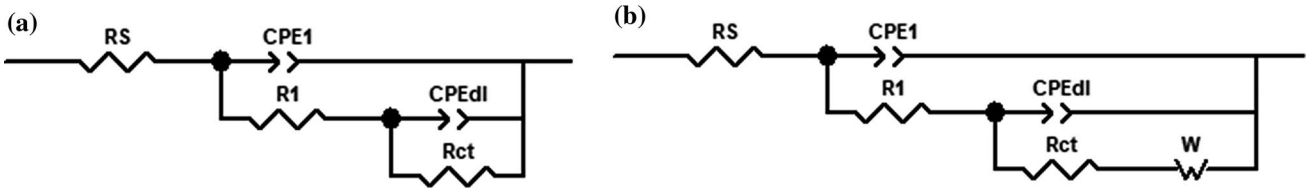

Figure 5 Electrical equivalent models, **a** and **b**, employed for fitting the EIS experimental data obtained after 2- and 24-h immersion, respectively.

Table 4 Parameters of the equivalent models obtained from fitting the EIS experimental data

Sample	Time(h)	Rs (Ω cm^2)	CPE1 Y0 (S.s^n /cm^2)	$n1$ $0<n<1$	$R1$ (Ω cm^2)	CPEdl Y0 (S.s^n /cm^2)	Ndl $0<n<1$	Rct (Ω cm^2)	Warburg Y0 (S.s$^{0.5}$ /cm^2)
TiMg cyl	2	236.2	6.94×10^{-4}	0.6593	98.34	1.59×10^{-4}	0.9811	822.1	–
	24	277.9	8.07×10^{-4}	0.5545	393.4	1.48×10^{-4}	1	118.6	1.26×10^{-4}
TiMg DI	2	225.1	1.36×10^{-3}	0.5748	43.6	1.32×10^{-6}	0.4915	2873	–
	24	307.2	3.4×10^{-6}	0.5015	502.9	2×10^{-4}	0.456	1002	3.13×10^{-4}

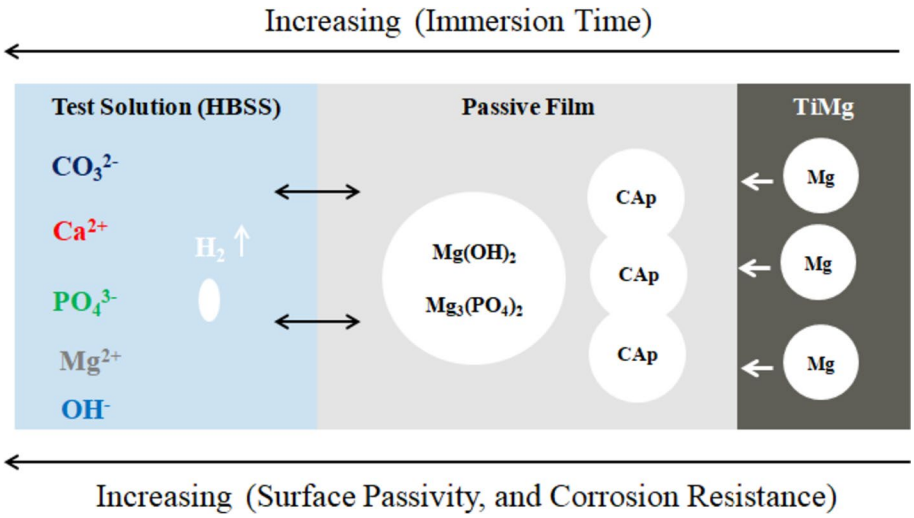

Figure 6 Systematic diagram of the proposed mechanism of degradation of the TiMg composite.

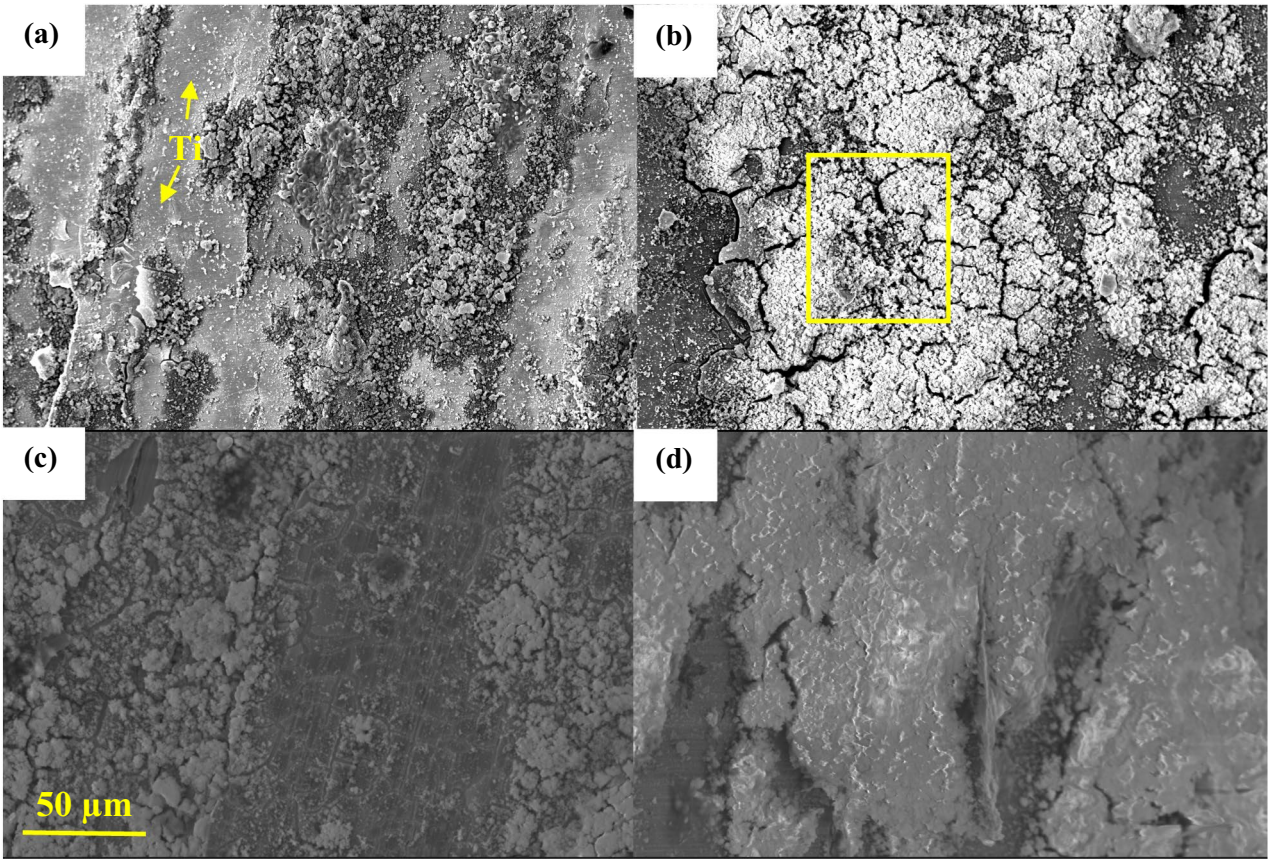

Element (wt%)	Oxygen (O)	Magnesium (Mg)	Titanium (Ti)	Carbon (C)	Phosphorus (P)	Calcium (Ca)	Sodium (Na)
Spectrum	42.97	5.82	7.95	5.43	13.56	21.02	3.26

Figure 7 SEM micrographs of surfaces of the TiMg cyl and TiMg DI samples after **a**, **c** 2- and **b**, **d** 24-h immersion in HBSS, respectively, along with results of elemental EDS analysis of the formed base film from the rectangle area. The arrows refer to the uncovered surface of Ti.

2-h exposure, as shown in Fig. 8. The formed film had a thickness of 59.8 ± 4.2 and 88.4 ± 3.2 µm after 2- and 24-h exposure, respectively. This behavior was consistent with the results of R_{corr} mentioned above. The EDS analysis confirmed that the surface of TiMg cyl after 24 immersion was passivated by a film enriched with Ca/P species (CAp). Moreover, the low percentage of Ti revealed that its surface was also covered in corrosion by-products. These SEM observations were in line with the electrochemical results outlined above.

Discussion

When a dental implant is placed in the oral environment, an electrochemical interaction between the implant material and the surrounding environment may occur. This interaction results in a release of metallic ions into the physiological environment and thus leads to the formation of corrosion by-products on the implant surface. This behavior may both result in damage to the surrounding tissues and impaired healing and trigger some adverse effects, such as allergy [31]. In an aqueous medium, Mg undergoes two chemical processes; dissolution of Mg [Eq. (1)] and hydrogen (H_2) evolution [Eq. (2)] [32].

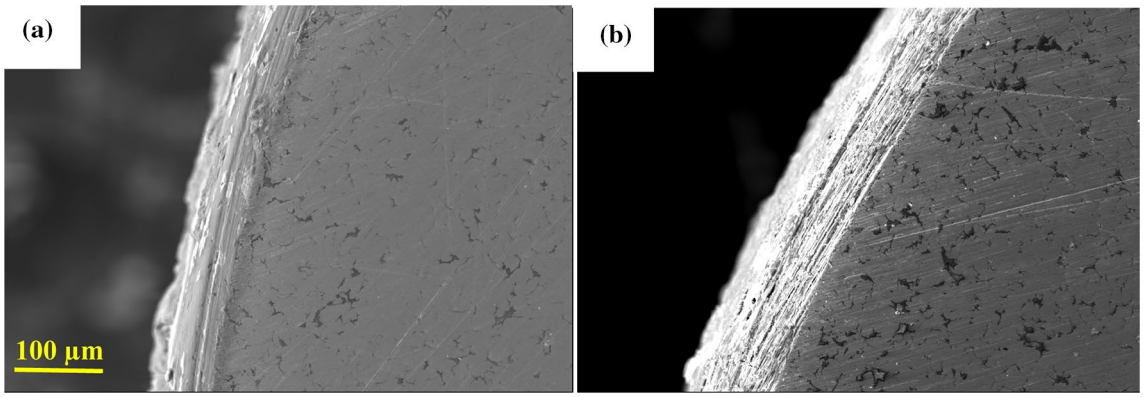

Figure 8 Representative cross-sectional SEM micrographs of TiMg cyl after **a** 2- and **b** 24-h exposure to HBSS.

$$\text{Anodic process: } Mg \rightarrow Mg^{2+} + 2e^{-} \quad (1)$$

$$\text{Cathodic process: } 2H_2O + 2e^{-} \rightarrow 2OH^{-} + H_2 \uparrow \quad (2)$$

$$\text{Overall reaction: } Mg + 2H_2O \rightarrow Mg(OH)_2 + H_2 \uparrow \quad (3)$$

According to [Eq. (3)], the surface of Mg is typically covered in $Mg(OH)_2$ with some micropores and defects caused by the H_2 evolution [33]. When Mg is coupled with Ti, the galvanic corrosion arises from a high difference in their standard electrode potential (− 2.356 vs. − 0.163, respectively) [20, 21]. The galvanic coupling intensifies the degradation of Mg, resulting in the H_2 evolution, which relatively curbs the protectiveness of the base film toward further degradation. Hence, it was significant to study the galvanic corrosion of the TiMg dental implant [22, 23].

Mg-containing materials generate an electrical potential when exposed to an electrolyte. This potential (OCP) reaches after a certain time of exposure to a value at which the tested sample is in a relatively steady state with its environment. For the OCP measurements, the initial abrupt increase was attributed to the formation and thickening of the base film formed on the surfaces of TiMg cyl and TiMg DI. Afterward, the slow increase in OCP revealed the growth of the formed film on the surfaces of the studied samples that promotes their corrosion resistance. The fluctuations in the OCP curves of TiMg cyl are difficult to interpret, but they were likely linked to surface characteristics and/or the occurrence of localized corrosion. For the PDP measurements, the cathodic branch of the polarization curve corresponds to a hydrogen evolution reaction due to the dissolution of Mg. TiMg cyl had a higher value of βc after 2-h immersion compared with that of TiMg DI, indicating a huge release of H_2 bubbles and a higher R_{corr} ensued. A prominent reduction in anodic current densities with increasing immersion time was observed, particularly for TiMg DI. This behavior revealed a stable passive film and high corrosion resistance. The difference in the Mg degradation of both samples after 24-h immersion was attributed to different geometries of the tested samples (cylindrical vs. threaded outer surface), surface roughness parameters, and the forms of Mg at the samples' surfaces. Although TiMg DI had slightly higher values of the surface roughness parameters than those of TiMg cyl, it showed lower R_{Corr}. This behavior was mostly attributed to a variation of the Mg component at the surface of TiMg DI compared with the one at the surface of TiMg cyl. In other words, TiMg DI of a complicated threaded design had two types of Mg, one type was arrayed along the direction of extrusion in the longitudinal direction, and the other one was in the form of an interconnected skeletal structure in the transversal direction. This behavior was consistent with [34], which revealed that the corrosion resistance of a rolled AZ80 magnesium alloy is very sensitive to the texture of Mg at the surface. Apart from that, as the exposure time extended, TiMg DI with a partially rough surface made the formed film relatively bound to its surface (Fig. 7d) and thus reduced the degradation of Mg.

EIS is a powerful method for evaluating the corrosion mechanism and the formed base film and its protectiveness [35–37]. To interpret the obtained EIS plots, it was necessary to propose an equivalent electrical circuit model that described all involved electrochemical reactions. The equivalent models consisted of different elements that precisely characterized the

corrosion behavior and mechanism. The employment of CPE instead of an ideal capacitor was necessary due to the inhomogeneous nature of the studied systems (i.e., rough surfaces and/or a variation of reaction rates). An electrical double layer (dl) represented the interface between the sample surface and its surrounding medium. This double layer was formed as ions from the medium were adsorbed onto the sample surface. Mg can electrolytically dissolve into the medium according to (Eq. 1); therefore, a charge transfer reaction occurred. Moreover, Mg^{2+} that diffused into the surrounding medium resulted in forming by-products on the sample surface, and such chemical diffusion processes can create a Warburg impedance, which depends on the frequency of the potential perturbation. At high frequencies, the Warburg impedance has small values since diffusing reactants don't have to move very far, whereas it has high values at low frequencies since the reactants have to diffuse farther [38]. The resistance of the formed film (R1) represented a barrier against ions migration, which reflected its protectiveness level [37, 39]. The capacitive response in the high frequency range was related to the base film, while the response in the low frequency range was linked to the double layer capacitance and the charge transfer resistance. After 2-h immersion, the capacitive loops that tended to close demonstrated the formation of a base film on the surfaces of the tested samples. The reaction was then controlled by a charge transfer process. As the immersion time extended, the H_2 evolution resulted in the formation of a relatively loose film, so the $n1$ values decreased. Moreover, TiMg cyl had higher values of ndl compared with those of TiMg DI. This was likely attributed to the variation of the geometry and surface roughness of the TiMg cyl and TiMg DI samples and the diffusion process through the formed film. After 24-h immersion, the high values of R1 for TiMg cyl and TiMg DI reflected the passive behavior and high corrosion resistance. The Warburg impedance was visible in the Nyquist plots after 24-h exposure that arose from the formation and dissolution of chemically non-stable by-products caused by the H_2 evolution. Therefore, as the exposure time extended, the polarization was due to a combination of kinetic and diffusion processes. The involved reaction was then controlled by both charge transfer and semi-infinite length diffusion processes, as shown in Fig. 5b.

As shown in Fig. 7, the formed by-products almost fully covered the surfaces of the tested samples after 24-h immersion in HBSS. The Mg component present at the surface obviously deteriorated, while Ti was protected because of the galvanic coupling. The TiMg cyl sample exposed to HBSS for 24 h was covered in a film composed of bioactive Ca/P species (CAp), ($Mg_3(PO_4)_2$), and $Mg(OH)_2$, as was confirmed by the EDS analysis and in our previous works [3–6]. The EIS results along with the SEM observations demonstrated that CAp formed the stable passive base that attached directly to the surface, while the other by-products started to dissolute as the exposure time extended and thus led to an increase in the mass transfer and chemical diffusion processes. As was reported in our previous works [3, 6], the biomimetic CAp boosted the cell survival and adhesion, and it is expected to promote the proliferation and osseointegration criteria [40].

This investigation revealed that the implant design, surface roughness, and forms of Mg at the surface crucially influenced the corrosion behavior and surface passivity. The accomplished results provided evidence that TiMg DI of a complicated threaded design had more stable passive film and higher corrosion resistance in HBSS compared with those of TiMg cyl of a cylindrical design. These results, along with the outstanding findings that were demonstrated in our previous works, revealed that TiMg DI has immense potential as a promising material for the fabrication of DI.

Acknowledgements

The authors thank MARTIKAN s.r.o for manufacturing the TiMg dental implants, Dr. Anna Kityk for her help with data analysis, and Prof. Martin Kusy for his help with the roughness measurements. Financial support from the SRDA APVV-20-0417 project is gratefully acknowledged. Furthermore, this work was performed during the implementation of the project Building-up Centre for advanced materials application of the Slovak Academy of Sciences, ITMS project code 313021T081 supported by Research & Innovation Operational Programme funded by the ERDF.

Author's contribution

AMHI was involved in conceptualization, methodology, investigation, and writing—original draft. MB was involved in supervision, funding acquisition, and project administration.

Funding

Open access funding provided by The Ministry of Education, Science, Research and Sport of the Slovak Republic in cooperation with Centre for Scientific and Technical Information of the Slovak Republic.

Data and code availability

Not applicable.

Declarations

Conflict of interest The authors declare that they have no conflict of interest.

Ethical approval Not applicable.

References

[1] Niinomi M (2001) Recent metallic materials for biomedical applications. Met Mater Trans A 32A:477–486

[2] Geetha M, Singh AK, Asokamani R, Gogia AK (2009) Ti based biomaterials, the ultimate choice for orthopaedic implants - a review. Prog Mater Sci 54:397–425

[3] Cetin Y, Ibrahim AMH, Gungor A, Yildizhan Y, Balog M, Krizik P (2020) In-vitro evaluation of a partially biodegradable TiMg dental implant: the cytotoxicity, genotoxicity, and oxidative stress. Materialia 14:100899

[4] Ibrahim AMH, Balog M, Krizik P, Novy F, Cetin Y, Svec P Jr, Bajana O, Drienovsky M (2020) Partially biodegradable Ti-based composites for biomedical applications subjected to intense and cyclic loading. J Alloys Compd 839:155663

[5] Balog M, Ibrahim AMH, Krizik P, Bajana O, Klimova A, Catic A, Schauperl Z (2019) Bioactive Ti + Mg composites fabricated by powder metallurgy: the relation between the microstructure and mechanical properties. J Mech Behav Biomed Mater 90:45–53

[6] Ibrahim AMH, Takacova M, Jelenska L, Csaderova L, Balog M, Kopacek J, Svastova E, Krizik P (2021) The effect of surface modification of TiMg composite on the in-vitro degradation response, cell survival, adhesion, and proliferation. Mater Sci Eng C 127:112259

[7] Makkar P, Sarkar SK, Padalhin AR, Moon BG, Lee YS, Lee BT (2018) In vitro and in vivo assessment of biomedical Mg–Ca alloys for bone implant applications. J Appl Biomater Funct Mater 16:126–136

[8] Gu XN, Xie XH, Li N, Zheng YF, Qin L (2012) In vitro and in vivo studies on a Mg–Sr binary alloy system developed as a new kind of biodegradable metal. Acta Biomater 8:2360–2374

[9] Galli S, Stocchero M, Andersson M, Karlsson J, He W, Lilin T, Wennerberg A, Jimbo R (2017) The effect of magnesium on early osseointegration in osteoporotic bone: a histological and gene expression investigation. Osteoporos Int 28(7):2195–2205

[10] Quezada-Castillo E, Aguilar-Castro W, QuezadaAlvan B (2019) Corrosion of galvanic pairs of dental alloys copper base with silver amalgams in artificial saliva. Matéria (Rio J.) 24(1):1–10

[11] Wang ZB, Hu HX, Zheng YG (2015) Determination and explanation of pH related critical fluoride concentration of pure titanium in acidic solutions using electrochemical methods. Electrochim Acta 170:300–310

[12] Wang ZB, Hu HX, Zheng YG, Ke W, Qiao YX (2016) Comparison of the corrosion behavior of pure titanium and its alloys in fluoride containing sulfuric acid. Corros Sci 103:50–65

[13] Frateur I, Cattarin S, Musiani M (2000) Electrodissolution of Ti and p-Si in acidic fluoride media: formation ratio of

oxide layers from electrochemical impedance spectroscopy. J Electroanal Chem 482:202–210
[14] Yang W, Liu Z, Huang H (2021) Galvanic corrosion behavior between AZ91D magnesium alloy and copper in distilled water. Corros Sci 188:109562
[15] Xiao K, Dong C, Wei D et al (2016) Galvanic corrosion of magnesium alloy and aluminum alloy by kelvin probe. J Wuhan Univ Technol Mater Sci 31(1):204–210
[16] Deshpande KB (2010) Validated numerical modelling of galvanic corrosion for couples: magnesium alloy (AE44)-mild steel and AE44-aluminium alloy (AA6063) in brine solution. Corros Sci 52(10):3514–3522
[17] Bai LJ, Kou G, Zhao K et al (2018) Effect of in-situ micro-arc oxidation coating on the galvanic corrosion of AZ31Mg coupled to aluminum alloys. J Alloys Compd 775:1077–1085
[18] Pan Y, Wu G, Cheng X et al (2015) Galvanic corrosion behaviour of carbon fibre reinforced polymer/magnesium alloys coupling. Corros Sci 98:672–677
[19] Song G, Johannesson B, Hapugoda S, StJohn D (2004) Galvanic corrosion of magnesium alloy AZ91D in contact with an aluminium alloy, steel and zinc. Corros Sci 46(4):955–977
[20] Bard AJ, Parsons B, Jordon J (eds) (1985) Standard potentials in aqueous solutions. Dekker, New York
[21] Milazzo G, Caroli S, Sharma VK (1978) Tables of standard electrode potentials. Wiley, London
[22] Arslan H, Çelikkan H, Örnek N et al (2008) Galvanic corrosion of titanium-based dental implant materials. J Appl Electrochem 38:853–859
[23] Hsu RW-W, Yang C-C, Huang C-A, Chen Y-S (2004) Electrochemical corrosion properties of Ti–6Al–4V implant alloy in the biological environment. Mater Sci Eng A 380(1–2):100–109
[24] Fajardo S, García-Galvan FR, Barranco V, Galvan JC, Batlle SF (2018) A critical review of the application of electrochemical techniques for studying corrosion of Mg and Mg alloys: opportunities and challenges. In: Tański T, Borek W, Król M (eds) Magnesium alloys-selected issue. IntechOpen, London
[25] Kirkland NT, Birbilis N, Staiger MP (2012) Assessing the corrosion of biodegradable magnesium implants: a critical review of current methodologies and their limitations. Acta Biomater 8:925–936
[26] King AD, Birbilis N, Scully JR (2014) Accurate electrochemical measurement of magnesium corrosion rates; a combined impedance, mass-loss and hydrogen collection study. Electrochim Acta 121:394–406
[27] Feliu S, García-Galvan FR, Llorente I, Diaz L, Simancas J (2017) Influence of hydrogen bubbles adhering to the exposed surface on the corrosion rate of magnesium alloys AZ31 and AZ61 in sodium chloride solution. Mater Corros 68:651–663
[28] Curioni M, Scenini F, Monetta T, Bellucci F (2015) Correlation between electrochemical impedance measurements and corrosion rate of magnesium investigated by real-time hydrogen measurement and optical imaging. Electrochim Acta 166:372–384
[29] Jamesh M, Kumar S, Sankara Narayanan TSN (2011) Corrosion behavior of commercially pure Mg and ZM21 Mg alloy in Ringer's solution–long term evaluation by EIS. Corros Sci 53:645–654
[30] https://www.martikan.eu/produkty/dentalne-implantaty/dent%C3%A1lny-implant%C3%A1t-mv-3,6-527-599
[31] Merrit K, Brown SA (1981) Hypersensitivity to metallic biomaterials, 2nd edn. CRC Press, Boca Raton
[32] Thomas S, Medhekar NV, Frankel GS et al (2015) Corrosion mechanism and hydrogen evolution on Mg. Curr Opin Solid State Mater Sci 19(2):85–94
[33] Wang L, Shinohara T, Zhang BP (2009) Corrosion behavior of AZ31 magnesium alloy in dilute sodium chloride solutions. ZairyotoKankyo 58(3):105–110
[34] Xiong Y, Yang Z, Zhu T, Jiang Y (2020) Effect of texture evolution on corrosion resistance of AZ80 magnesium alloy subjected to applied force in simulated body fluid. Mater Res Express 7:015406
[35] Liu Y, Wang Z, Ke W (2014) Study on influence of native oxide and corrosion products on atmospheric corrosion of pure Al. Corros Sci 80:169–176
[36] Cui ZY, Li XG, Xiao K, Dong CF (2013) Atmospheric corrosion of field-exposed AZ31 magnesium in a tropical marine environment. Corros Sci 76:243–256
[37] Cui Z, Li X, Zhang H, Xiao K, Dong C, Liu Z, Wang L (2015) Atmospheric corrosion behavior of 2A12 Aluminum alloy in a tropical marine environment. Adv Mater Sci Eng 2015:17
[38] Nguyen TQ, Breitkopf C (2018) Determination of diffusion coefficients using impedance spectroscopy data. J Electrochem Soc 165:E826–E831
[39] Ma Y, Li Y, Wang F (2008) The effect of β-FeOOH on the corrosion behavior of low carbon steel exposed in tropic marine environment. Mater Chem Phys 112(3):844–852
[40] Duygulu O, Kaya AA, Oktay G, Sahin FC (2007) Diffusion bonding of magnesium, zirconium and titanium as implant material. Mater Sci Forum 546–549:417–420